Submicrometer-Gap Thermionic Power Generation Based on Comprehensive Modeling of Charge and Thermal Transport

Devon Jensen[1,2,†] A. N. M. Taufiq Elahi[1,†] Mohammad Ghashami[3] and Keunhan Park[1,*]

[1]*Department of Mechanical Engineering, University of Utah, Salt Lake City, Utah 84112, USA*
[2]*Advanced Cooling Technologies, Inc., Lancaster, Pennsylvania 17601, USA*
[3]*Mechanical & Materials Engineering Department, University of Nebraska-Lincoln, Lincoln, Nebraska 68588, USA*

This paper presents the comprehensive performance analysis of thermionic power generation when the interelectrode vacuum gap shrinks to the submicron range. Although reducing the vacuum gap has been suggested as an effective approach to mitigate space-charge accumulation in thermionic-energy-conversion (TEC) devices, previous theoretical works have predicted the optimal gap distance in the single-digit micrometer range. However, we demonstrate that nanoscale charge and thermal interactions between thermionic electrodes, such as Schottky barrier lowering due to image charge perturbation and near-field enhanced radiative heat transfer, significantly affects the TEC performance within the submicron vacuum gap. Carefully conducted energy-balance analysis reveals that submicron-gap TEC at $d \approx 700$ nm can produce an approximately fourfold increase in power output with a higher energy conversion efficiency than micron-gap TEC under the same operating condition. In addition, significant thermionic and near-field radiative heating of the collector in the submicron-gap TEC system can be beneficially used to further enhance the power output and efficiency by combining with a bottom-cycle heat engine. We believe that the present work provides a theoretical framework for submicron-gap thermionic power generation as a promising energy recycling scheme for high-quality heat sources.

I. INTRODUCTION

Thermionic energy conversion (TEC) is a direct heat-to-electrical power-generation scheme, configured with a thermionic emitter (or cathode) and collector (or anode) separated by a vacuum space [1,2]. When the emitter is heated to a high temperature, typically over 1400 K [2], electrons with higher energies than the emitter's work function evaporate from the surface. When a thermionic cell is connected to an electrical load, the emitted electrons are swept to the collector and flow through the load to generate electric power. While thermophotovoltaic (TPV) and thermoelectric heat engines also convert heat to electric power, TEC devices are advantageous at heat-source temperatures above 1400 K. First, the theoretical efficiency limit of TEC is higher than those of TPV and thermoelectric heat engines at high heat-source temperatures [3]. Second, thermionic power generation avoids some of the technical challenges faced in TPV and thermoelectric schemes at high temperatures, such as mitigating

a large dark current in a TPV cell and sustaining a large temperature gradient in a thermoelectric cell [4–6].

Despite these appealing features, TEC has not been widely adopted due to nonideal factors that lower actual energy conversion efficiency. In the 1960s, Wilson and Becker reported thermionic conversion efficiencies between 5% and 20% for tungsten-nickel and renium-nickel electrodes operating above 2000 K [7,8]. However, energy conversion efficiencies of contemporary TEC devices still remain below approximately 15% mainly due to high electrode work functions [9]. For example, the work function of tungsten, routinely used for thermionic electrodes, is approximately 4.5 eV [10], which is too large to obtain sufficient power generation and efficiency in the temperature range from 1000 to 2000 K. Over the years, several methods have been proposed to lower work functions, such as barium surface coatings [11], atomic surface modification [12–14], and surface nanotexturing [15]. However, when the electrostatic field between the electrodes is not strong enough to immediately attract emitted electrons to the collector, lower work-function electrodes do not necessarily improve thermionic performance. Under a weak electrostatic field, electrons accumulate between

---

*kpark@mech.utah.edu
†These authors contributed equally to this work.

the electrodes, inducing a repulsive force that increases the energy required for electron emission [2,16–18]. This negative space-charge effect has been mitigated by filling the vacuum space with positive ions [2,19]. However, electron scattering upon collisions with positive ions and neutralized atoms lowers the overall system efficiency. Although Meir *et al.* [20] proposed inserting a positively biased micromesh gate between the electrodes to accelerate electrons to the collector, fabricating the gate structure between the emitter and collector is not an easy task, and a magnetic field should be applied parallel to the averaged electron trajectories to reduce the current lost to the gate. A recent study proposed using two-dimensional (2D) materials such as graphene for magnetic-field-free gate electrodes [21]. However, 2D material electrodes are not mass producible for TEC mainly due to technical difficulties in large-scale synthesis of high-quality 2D materials.

Another feasible approach to mitigate the space-charge effect is to reduce the vacuum-gap distance between the emitter and collector. Hatsopoulos and Gyftopoulos [2] claimed that reducing the interelectrode vacuum gap can suppress space-charge accumulation by increasing the electric field in the vacuum space. Since then, previous works have demonstrated potential benefits of reducing the interelectrode vacuum gap for thermionic refrigeration [22,23] and power generation [24–27]. However, most of the previous works focused only on the sub-100-nm vacuum-gap range, thereby ignoring the negative space-charge effect [22–25,27]. Lee *et al.* [26] considered the gap-dependent space-charge effect and near-field thermal radiation to calculate the optimal emitter-collector gap for TEC. However, they overlooked Schottky barrier lowering due to the image charge effect and heat rejection from the TEC collector to the environment, and evaluated the TEC performance from the efficiency standpoint only. As a result, they suggested an optimal efficiency gap between 900 nm and 3 μm over a wide range of operating conditions for cesiated tungsten electrodes. This design principle has been applied to recent experimental and theoretical works on thermionic power generation, which have focused on micron-sized gap distances [5,11,18,28,29].

In the present paper, we report a theoretical study that challenges the long-believed design principle of a TEC system by demonstrating compelling advantages of further reducing the interelectrode vacuum gap to the submicrometer regime. Charge- and thermal-transport processes across a reduced vacuum gap are rigorously modeled by considering reduced gap effects, such as image-charge potentials, electron tunneling, and near-field thermal radiation, in a comprehensive manner. Systematic energy balance analysis is the key to understand thermionic and radiative energy transfer in the thermionic cell and its heat rejection to the environment, from which the thermionic power output and energy conversion efficiency can be accurately calculated. The obtained results reveal that if optimized, a submicrometer vacuum gap permits the best TEC performance from both power output and efficiency standpoints. In addition, our work investigates possibilities to further improve the TEC performance by topping a TEC device in a combined cycle configuration.

II. MODELING

A. Charge-transport processes

Figure 1(a) illustrates the schematics and energy diagram of a vacuum TEC system that consists of a thermionic emitter with a work function Φ_E and a collector with a work function Φ_C, connected to an electrical load. In the present work, the reference point for the electron energy is set to the Fermi level of the emitter material. When the emitter temperature is elevated to T_E, electrons are emitted and travel to the collector at temperature T_C by thermionic emission and quantum electron tunneling. The net current density carried by electrons across the interelectrode gap can be calculated as $J_e = J_{TE} + J_{QE}$, where J_{TE} is the net thermionic current density and J_{QE} is the net electron-tunneling current density. In general, the current density from electrode i can be expressed as [17,30]

$$J_i = q \int \mathcal{T}(E_x) N_i(E_x, T_i) dE_x, \tag{1}$$

where i is either the emitter (E) or the collector (C), q is the electron charge, $\mathcal{T}(E_x)$ is the electron transmission probability, and E_x is the electron energy corresponding to the emission pathway normal to the surface. $N_i(E_x, T_i)$ is the supply function of electrode i, denoting the number of electrons incident on a unit area within the electrode in unit time with energies between E_x and $E_x + dE_x$ at temperature T_i.

When electrons have an E_x higher than the maximum potential barrier W_{max}, they are thermionically emitted from the electrode and travel through the vacuum space with a transmission probability of $\mathcal{T}(E_x) = 1$. Since electron energies required for thermionic emission are much higher than the Fermi level [i.e., $E_{F,i}$ in Fig. 1(a)], the supply function can be approximated as $N_i(E_x, T_i) = (m_e k_B T_i / 2\pi^2 \hbar^3) \exp[-(E_x - E_{F,i})/k_B T_i]$ from the Maxwell-Boltzmann distribution [17]. Here, k_B and $\hbar = h/2\pi$ are the Boltzmann constant and the reduced Planck constant, respectively. J_{TE} is then derived by integrating Eq. (1) from $E_x = W_{max}$ to infinity to yield the Richardson-Dushman equation:

$$J_{TE} = J_{TE,E} - J_{TE,C} = A T_E^2 \exp\left[\frac{-W_{max}}{k_B T_E}\right]$$
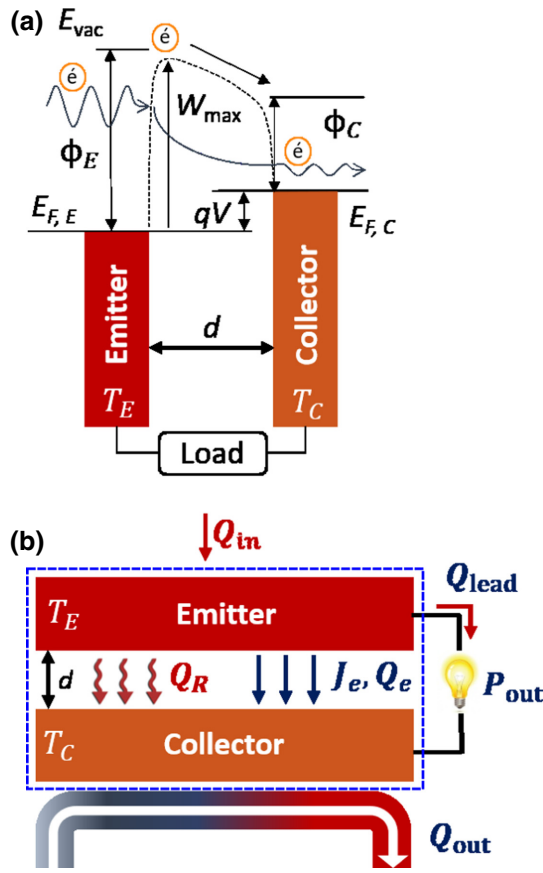$$- A T_C^2 \exp\left[\frac{-(W_{max} - qV)}{k_B T_C}\right], \tag{2}$$

FIG. 1. (a) Schematic diagram of the thermionic potential profile across a submicron vacuum gap. The electric field between the electrodes that shapes the potential profile is caused by the work-function difference, the voltage drop over the load, and the image-charge potential. The resulting electric current across the vacuum gap occurs classically (thermionic) and quantum mechanically (electron tunneling). (b) TEC device schematic. In addition to charge transport due to electrons, heat is transferred across a vacuum space by electrons and thermal radiation, partly converted to electric power and the remaining rejected to a room-temperature reservoir.

where $A = 4\pi m_e k_B^2 q/h^3$ is the Richardson constant and V is the operating voltage. When the interelectrode vacuum gap is reduced to the nanoscale, electrons can also tunnel through the vacuum gap although their energy is below $W_{\max}$. For quantum electron tunneling, the transmission probability is no longer unity but approximated as $\mathcal{T}(E_x) = \exp[-\theta(E_x)]$, where $\theta(E_x)$ can be written as the following equation based on the Wentzel-Kramers-Brillouin (WKB) approximation [22,25,27,31–34]:

$$\theta(E_x) = \frac{\sqrt{8m_e}}{\hbar} \int_{x_1}^{x_2} \sqrt{W(x) - E_x}\, dx. \qquad (3)$$

Here, x_1 and x_2 are the locations at which E_x equals the local potential barrier $W(x)$, designating the thickness of

the electron tunneling barrier at E_x. In addition, the Fermi-Dirac distribution should be used for the supply function to yield $N_i(E_x, T_i) = (m_e k_B T_i/2\pi^2\hbar^3)\ln\{1 + \exp[-(E_x - E_{F,i})/k_B T_i]\}$ for electron tunneling [33]. Therefore, the net electron-tunneling current density can be written as

$$J_{QE} = J_{QE,E} - J_{QE,C}$$
$$= q\int_{-\infty}^{W_{\max}} \mathcal{T}(E_x)\,[N_E(E_x, T_E) - N_C(E_x - qV, T_C)]\, dE_x. \qquad (4)$$

For the accurate calculation of the net current density, it is crucial to obtain the potential barrier profile $W(x)$ and determine $W_{\max}$ from the obtained profile. Within the electrostatic framework, the potential barrier profile can be written as

$$W(x) = W_e(x) + W_{IC}(x). \qquad (5)$$

Here, $W_e(x)$ is the potential barrier profile when electrons exist in the vacuum space while $W_{IC}(x)$ denotes the image-charge perturbation. In general, electrons accumulated in the vacuum space build up negative charge to impede further emission of electrons from the electrode surfaces. This negative space-charge effect on the potential barrier profile can be calculated by solving Poisson's equation [1,2,16,17]:

$$\frac{d^2 W_e}{dx^2} = -\frac{q^2 n_e(x)}{\varepsilon_0}, \qquad (6)$$

where ε_0 is the permittivity of free space, x is the position between the emitter surface ($x = 0$) and the collector surface ($x = d$), and $n_e(x)$ is the local number density of electrons in the vacuum space. Since $n_e(x)$ is implicitly coupled with $W_e(x)$ through an electron distribution function, we numerically solve Eq. (6) by assuming that electrons are emitted with the half-Maxwellian distribution function in the normal direction to the electrode surfaces and travel through the vacuum space without collision. The boundary conditions are $W_e(0) = \Phi_E$ and $W_e(d) = \Phi_C$ while $dW_e/dx = 0$ at $x = x_{\max}$ for $0 \le x_{\max} \le d$. The framework for the numerical calculation of Eq. (6) is described in Refs. [2,16] and is not repeated here. If negative charges are not present in the interelectrode space (i.e., $n_e = 0$), the potential barrier becomes ideal with a linear profile in terms of the electrode work functions (Φ_E and Φ_C) and the operating voltage as follows [35,36]:

$$W_{id}(x) = \Phi_E - (\Phi_E - \Phi_C - qV)\left(\frac{x}{d}\right) \qquad (7)$$

Therefore, the space-charge effect on the potential barrier profile can be expressed as $W_{SC}(x) = W_e(x) - W_{id}(x)$. In contrast, $W_{IC}(x)$ lowers the potential barrier due to

electrostatic interactions between image charges in both electrodes and electrons in the vacuum space. The image-charge effect can be calculated by [36]

$$W_{IC}(x) = \frac{q^2}{16\pi\varepsilon_0 d}\left[-2\Psi(1) + \Psi\left(\frac{x}{d}\right) + \Psi\left(1-\frac{x}{d}\right)\right],$$

(8)

where $\Psi = d\log\Gamma(x)/dx$ is the digamma function. It should be noted that the above equation is essentially identical to the image potential equation in other works [22,23,25,27,35].

For macroscale vacuum gaps, $W_{SC}(x)$ is the dominant factor that increases $W(x)$ (and subsequently W_{max}) while $W_{IC}(x)$ only rounds off the potential barrier near the electrode surfaces. However, as the vacuum gap decreases, the electric field strength grows between the electrodes to suppress the space-charge effect [i.e., $W_e(x) \approx W_{id}(x)$]. Meanwhile, the electric field is further enhanced due to strong interactions between real and image charges across the small gap distance, which lowers $W(x)$ below the ideal profile and reduces its effective thickness at E_x (i.e., $x_2 - x_1$) [17].

B. Energy-balance analysis

As illustrated in Fig. 1(b), heat input from a heat source to the thermionic emitter is balanced by energy transfer by electrons (Q_e), thermal radiation (Q_R), and heat conduction through the electrical leads (Q_{lead}). Some of the energy transferred by electrons is then used to generate electric power in the external load (P_{out}) while the remainder is converted to heat in the collector. The thermionic-energy-conversion efficiency can be expressed as [16]

$$\eta = \frac{P_{out}}{Q_{in}} = \frac{P_{out}}{Q_e + Q_R + Q_{lead}}.$$

(9)

Here, the power output at the external load is calculated by $P_{out} = J_e[V - V_{lead}]$, where J_e is the net current density due to thermionic emission and electron tunneling, and $V_{lead} = J_e R_{lead}$ is the voltage drop across the electrical leads with resistance R_{lead}. If the heat and power losses by the electrical leads are ignored (i.e., $Q_{lead} = 0$ and $P_{lead} = J_e V_{lead} = 0$), the thermionic-energy-conversion efficiency can be simplified as $\eta = J_e V/(Q_e + Q_R)$, which is used to optimize the operating voltage as is further discussed in Fig. 3.

The electron-carried energy flux across a submicron-sized vacuum gap includes thermionic emission and electron tunneling, i.e., $Q_e = Q_{TE} + Q_{QE}$, where

$$Q_{TE} = \frac{1}{q}[J_{TE}W_{max} + 2k_B(J_E T_E - J_C T_C)]$$

(10)

is the thermionic energy flux [26]. Here, the second term denotes the kinetic energy carried away from each electrode by electrons [16]. The electron-tunneling energy flux can be calculated by [22,25]

$$Q_{QE} = \int_{-\infty}^{W_{max}} \mathcal{T}(E_x)[(E_x + k_B T_E)N_E(E_x, T_E) \\ - (E_x + k_B T_C)N_C(E_x - qV, T_C)]dE_x.$$
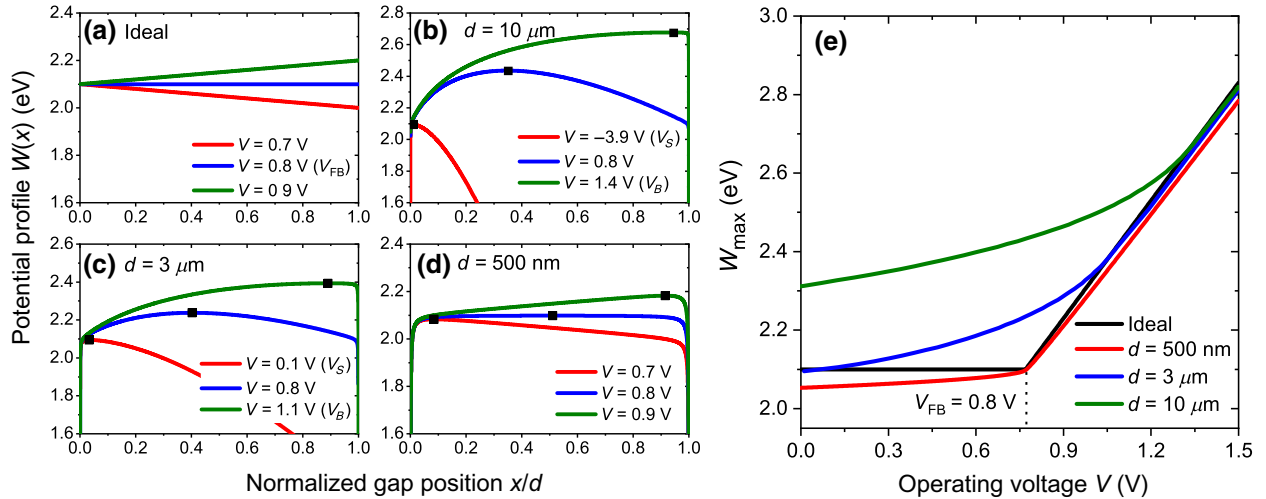
(11)

FIG. 2. Potential barrier profiles, $W(x)$, and the maximum potential W_{max} for three vacuum gaps ($d = 500$ nm, 3 μm, and 10 μm) when $T_E = 1575$ K ($\Phi_E = 2.10$ eV) and $T_C = 1000$ K ($\Phi_C = 1.33$ eV). (a) Ideal potential profiles at different operating voltages, where the flat-band voltage (V_{FB}) is 0.8 V. (b),(c) Realistic potential profiles for $d = 10$ μm and $d = 3$ μm, respectively, present the increase of the potential barrier due to the space-charge effect. In the figures, V_B and V_S denote the Boltzmann voltage and saturation voltage, respectively. (d) Potential profiles for $d = 500$ nm, which is slightly lower than the ideal profiles due to image-charge effect. (e) The relation between W_{max} and the operating voltage for different gap distances. The locations of W_{max} are marked with solid square points in (b)–(d).
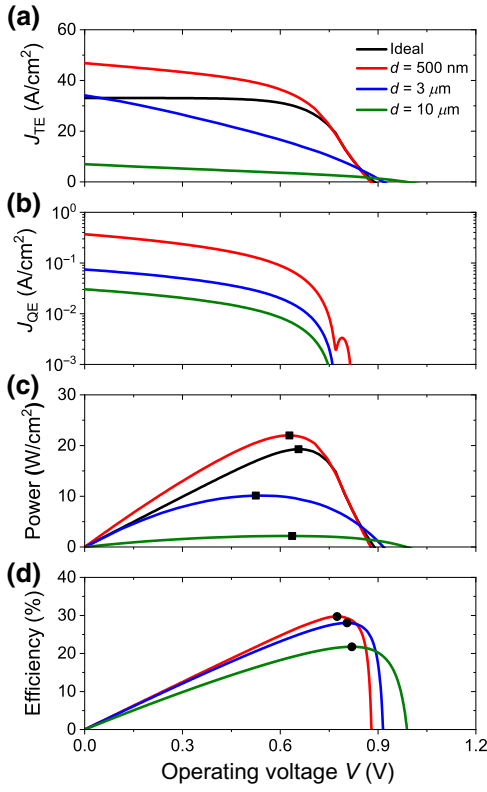
FIG. 3. (a) The net thermionic current density (J_{TE}), (b) the electron-tunneling current density (J_{QE}), (c) the power density, and (d) the energy conversion efficiency curves as a function of the operating voltage for three vacuum gaps ($d = 500$ nm, 3 μm, and 10 μm) under the same operating condition as Fig. 2. The solid square and circle marks in (c),(d) denote the maximum power and efficiency operation points, respectively.

The radiative heat transfer across a submicron vacuum gap should have near-field enhancement due to photon tunneling of thermally excited evanescent electromagnetic waves [37]. The net near-field radiative heat flux from the emitter to the collector can be calculated by the following equation [37–39]:

$$Q_R = \frac{1}{\pi^2} \int_0^\infty d\omega [\Theta(\omega, T_E) - \Theta(\omega, T_C)]$$
$$\times \int_0^\infty Z(k_\parallel, \omega) k_\parallel dk_\parallel, \qquad (12)$$

where $\Theta(\omega, T_i) = \hbar\omega/[\exp(\hbar\omega/k_B T_i) - 1]$ is the mean energy of a Planck oscillator at angular frequency ω, and $k_\parallel$ is the wavevector component parallel to the surface. $Z(k_\parallel, \omega)$ is the exchange function that can be formulated by the dyadic Green's function within the fluctuational electrodynamics framework. The detailed formulation of $Z(k_\parallel, \omega)$ for a three-layer configuration with a semi-infinite emitter and collector can be found in previous works [37–39] and is not repeated here. The conduction heat loss

through the electrical lead is calculated by [16,26]

$$Q_{lead} = \frac{L}{2R_{lead}}(T_E^2 - T_C^2) - \frac{J_e^2 R_{lead}}{2}, \qquad (13)$$

where $L = 2.24 \times 10^{-8}$ WΩ/K^2 is the Lorentz number and R_{lead} is the electrical resistance of the leads. It should be noted that Eq. (13) considers heat conduction through the leads under the joule heating. In the present work, the lead resistance is optimized by maximizing the efficiency (i.e., $\partial\eta/\partial R_{lead} = 0$) [16]. Heat rejection from the collector to maintain T_C is simply modeled as $Q_{out} = h_\infty(T_C - T_\infty)$, where h_∞ is the convection-heat-transfer coefficient. T_∞ is the environmental temperature and set to 300 K to evaluate the overall heat-transfer rate to the environment. Therefore, the amount of heat rejection and the corresponding heat-transfer coefficient can be calculated by the energy balance of the TEC (i.e., $Q_{out} = Q_{in} - P_{out}$).

In the present study, the TEC system is configured with tungsten-barium-oxygen (W-Ba-O) electrodes, which can lower the work function down to approximately 1 eV by controlling the ratio of adsorbed Ba and O atoms [40]. The emitter temperature is set to $T_E = 1575$ K by considering the operation of a dispenser cathode for thermionic emission [41]. The optimal work function of a thermionic electrode should be in the range of $600 < T/\Phi < 800$ [2], from which we select the work functions of both electrodes to satisfy $\Phi = T/750$. This design point yields $\Phi_E = 2.10$ eV for the emitter and $\Phi_C = 1.33$ eV when the collector temperature is maintained at $T_C = 1000$ K. The dielectric functions of the emitter and the collector are calculated based on tungsten electrodes using the Drude model, which can be written as $\epsilon(\omega, T_i) = 1 - \sigma_{0,i}/[\tau_i\epsilon_0(\omega^2 + i\omega/\tau_i)]$. Here, $\sigma_{0,i}$ is the dc conductivity [42] and τ_i is the electron relaxation time of electrode i [26,43], both of which are considered to be temperature dependent. Two design-point scenarios are considered based on maximum power output and maximum energy conversion efficiency to show the advantage of submicron-gap thermionic power generation. In addition, we also investigate the off-design performance of the optimized submicron-gap TEC device when the convective-heat-transfer coefficient for heat rejection changes.

III. RESULTS AND DISCUSSION

As mentioned in the modeling section, accurate calculation of the potential profile $W(x)$ is crucial for the reliable performance analysis of thermionic power generation. Figure 2 shows $W(x)$ as a function of the normalized gap position, x/d, and the corresponding W_{max} as a function of the operating voltage for different gap distances. For the ideal case with $\Phi_E = 2.10$ eV and $\Phi_C = 1.33$ eV, $W(x)$ exhibits a linear profile across the vacuum gap: see Fig. 2(a). As shown in Fig. 2(e), the resulting W_{max}
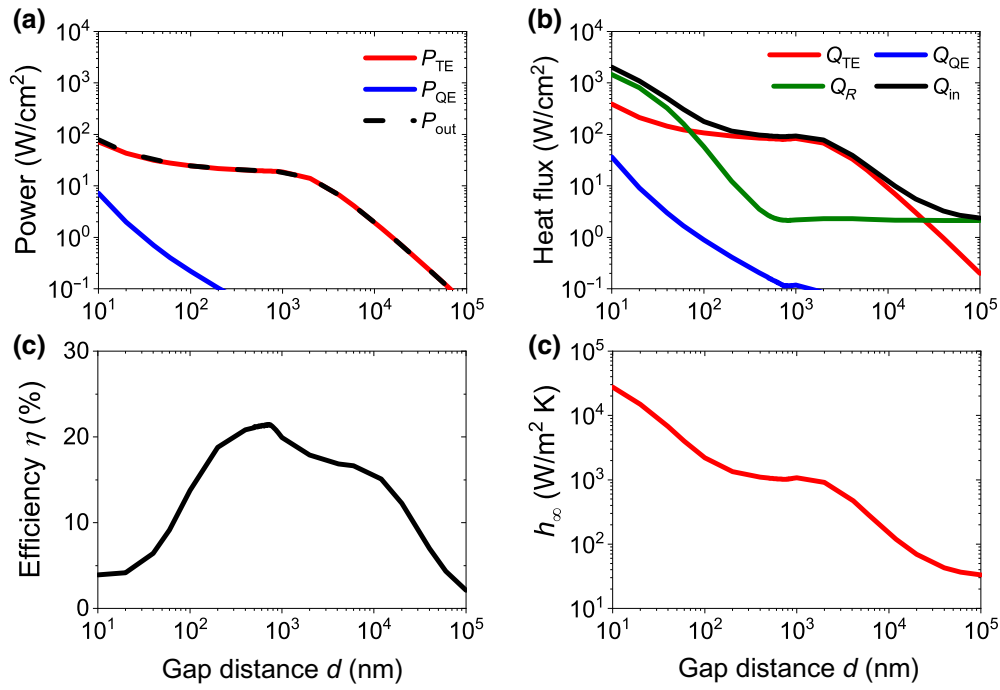
FIG. 4. The gap-dependent TEC performance characteristics operating at constant emitter and collector temperatures ($T_E = 1575$ K and $T_C = 1000$ K). (a) The maximum power density (black dashed) due to thermionic emission (red) and electron tunneling (blue). (b) The total heat flux across the vacuum gap (black) due to thermionic emission (red), electron tunneling (blue), and thermal radiation (green). (c) The resulting energy conversion efficiency and (d) the required convective-heat-transfer coefficient of a cooling fluid to maintain a constant $T_C = 1000$ K demonstrate the optimum gap distance for the given operation condition is in the range of 300 nm $\lesssim d \lesssim 1$ μm.

remains constant at Φ_E as the operating voltage increases to the flat-band voltage [i.e., $V_{FB} = (\Phi_E - \Phi_C)/q = 0.77$ V], and linearly increases with further increase of the operating voltage (i.e., $W_{max} = \Phi_C + qV$). However, when the thermionic electrodes are separated by microscale gap distances as shown in Figs. 2(b) and 2(c), the accumulation of negative charges in the vacuum space causes a paraboliclike potential energy profile with W_{max} greater than the ideal case. Besides the flat-band voltage, potential profiles at the Boltzmann voltage (V_B) and the saturation voltage (V_S) are also shown in Figs. 2(b) and 2(c) to better describe the dependence of the potential profile on the operating voltage. For $V > V_B$, charge transport is severely impeded by a high potential barrier near the collector surface to generate insignificant thermionic power. When the operating voltage is applied below the saturation voltage limit (i.e., $V < V_S$), electrons are accelerated by the electric field across the vacuum gap to yield W_{max} smaller than the ideal value. However, V_S is typically negative for microscale gaps, making the acceleration regime inadequate for thermionic power generation. When the vacuum gap is in the submicrometer range as shown in Fig. 2(d), the potential profiles become similar to the ideal profiles due to the suppression of the space-charge effect. Moreover, the image-charge effect accelerates electrons in

the entire operating voltage range, further reducing W_{max} below the ideal curve: see $d = 500$ nm in Fig. 2(e).

Based on the potential profile and W_{max}, the net thermionic and tunneling current densities (J_{TE} and J_{QE}, respectively) are calculated and plotted in Figs. 3(a) and 3(b). The ideal J_{TE} curve is flat up to $V \approx 0.75V_{FB}$, and exponentially decays for higher operating voltages. For microscale gap distances (e.g., $d = 3$ μm and 10 μm), the current-density values are significantly diminished due to the negative space-charge effect. In contrast, a submicron vacuum gap (i.e., $d = 500$ nm) generates a higher current density than the ideal J-V curve due to the image-charge effect, which is consistent with W_{max} in Fig. 2(e). The net tunneling current density exponentially decays as the operating voltage increases, with a steeper slope at higher voltages. Although J_{QE} increases as d shrinks into the submicron range, its contribution to total power generation is about 2 orders of magnitude smaller than J_{TE}. Figures 3(c) and 3(d) show the power density and efficiency curves as a function of the operating voltage when the electrical lead effects are ignored. From these results, operating voltages can be optimized to yield the maximum power or efficiency as design points. The solid square points marked in Fig. 3(c) denote the operating voltages yielding the maximum power outpsut, V_{max}, which are located

at approximately 0.6 V although the exact value depends on the gap distance. On the other hand, the solid circular points in Fig. 3(d) suggest that V_{max} should be set at approximately 0.8 V for the maximum efficiency operation. It should be noted that Fig. 3(d) does not include the ideal curve because the ideal efficiency changes for different gap distances due to the effect of gap-dependent near-field radiative heat transfer onto the efficiency.

Figure 4 shows the gap-dependent performance of the TEC system based on maximum power generation when $T_E = 1575$ K ($\Phi_E = 2.10$ eV) and $T_C = 1000$ K ($\Phi_C = 1.33$ eV). It should be noted that heat and power losses due to the electrical leads are considered for Fig. 4 and afterwards: see Fig. S1 and related discussion in the Supplemental Material for more information about the lead loss effects [44]. The net thermionic power density P_{TE} increases by more than 2 orders of magnitude as the gap distance decreases, from less than 0.05 W/cm² at $d = 100$ μm to 19.8 W/cm² at $d = 500$ nm, indicating the eradication of space charges by the increased field strength across the smaller gap. The observed gradual increase of P_{TE} in the submicron-sized gap regime is due to the image-charge effect. The tunneling power density (P_{QE}) also increases with the decreasing gap but contributes no more than approximately 6% of the total power output at $d = 10$ nm, suggesting that the electron-tunneling effect can be ignored unless an extremely small gap is to be considered. Conversely, Fig. 4(b) shows the heat flux by electrons and thermal radiation. Both the thermionic heat flux (Q_{TE}) and the electron-tunneling heat flux (Q_{QE}) follow similar trends to their respective power-density curves in Fig. 4(a). Therefore, thermionic emission is the dominant heat-transfer mechanism in the vacuum-gap range from approximately 300 nm to approximately 10 μm. On the other hand, the near-field enhancement of radiative heat transfer (Q_R) significantly increases the total heat flux (Q_{in}) for vacuum gaps smaller than 100 nm. In Fig. 4(c), the energy conversion efficiency exhibits a maximum of 21.5% ($P_{\text{out}} = 19.3$ W/cm²) at $d = 730$ nm alongside a shoulder in the micrometer gap range. The convection-heat-transfer coefficient h_∞ required to maintain the collector temperature at 1000 K is shown in Fig. 4(d). The obtained results suggest that 300 nm $\lesssim d \lesssim 1$ μm should be the optimal range for high-efficiency vacuum gap TECs while requiring h_∞ on the order of 1000 W/m² K for thermal management, which is a reasonable cooling load achievable with single-phase liquid convection [45].

It should be noted that the optimal gap distance obtained in Fig. 4 is based on the maximum power design point: see Fig. 3(c). However, designing the TEC device based on the maximum efficiency as shown in Fig. 3(d) may result in different TEC performance and an alternate optimal configuration. Figure 5 compares gap-dependent total power output and energy conversion efficiency for the two design perspectives. When the maximum efficiency is considered
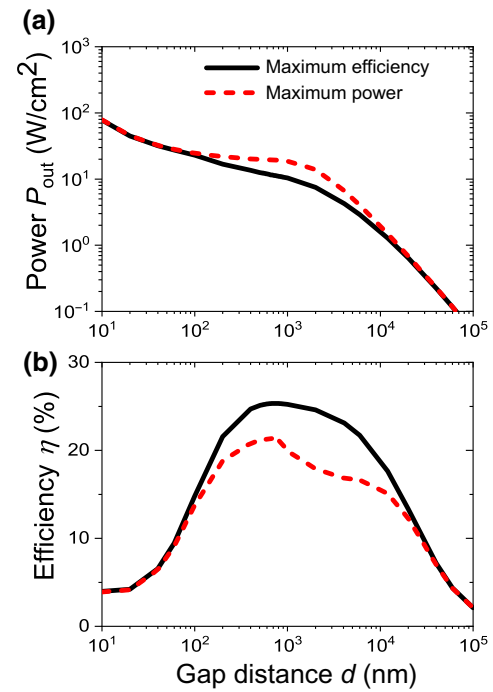

FIG. 5. (a) Total output power and (b) conversion efficiency when comparing the TEC conditions of maximum power output and maximum efficiency. For both conditions, the greatest power output and efficiency occurs at gaps below 1 μm.

as the design perspective, the calculated efficiency reaches a maximum of 25.3% at $d = 720$ nm, which is higher than that predicted from the maximum power perspective (i.e., $\eta_{\text{max}} = 21.5\%$ at $d = 730$ nm). At the optimal gap distance, the maximum efficiency-based design generates a power output of 11.3 W/cm², which is about 40% smaller than the output from the maximum power-based design (i.e., 19.3 W/cm²). Hence, a TEC device should be carefully designed to make a good balance between the power output and efficiency. Nevertheless, both design perspectives predict the optimal gap distance in the submicron range when charge and thermal transports are comprehensively modeled in the energy-balance analysis of a TEC device. While the present study considers only one design condition at $T_E = 1575$ K and $T_C = 1000$ K, the emitter and collector temperature effects on thermionic power generation are further discussed in the Supplemental Material (Figs. S2 and S3) [44].

Although the TEC device is optimized as described in Fig. 5, its performance may be significantly altered if the device is operated away from the design point. Figures 6(a) and 6(b) show the collector temperature and the corresponding power and efficiency as a function of the convection-heat-transfer coefficient of the cooling fluid. As the heat-transfer coefficient decreases from the design point (10^3 W/m² K) to 10^2 W/m² K, the collector temperature is elevated from approximately 1000 to 1555 K.
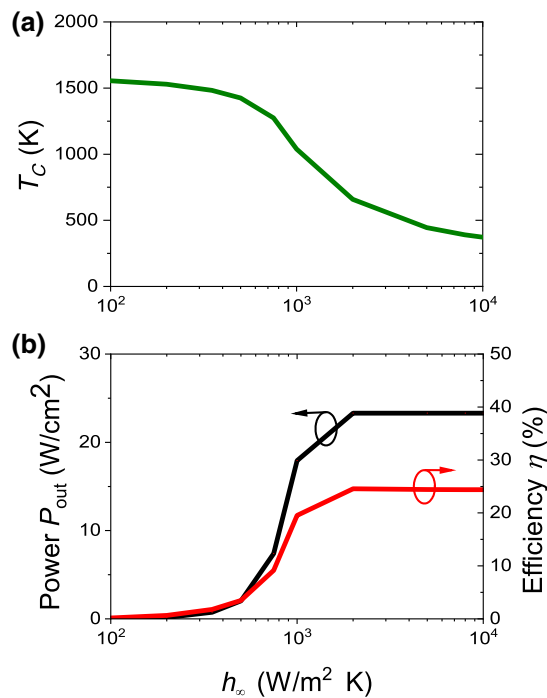
FIG. 6. (a) Collector temperature and (b) resultant power and efficiency as a function of the convective-heat-transfer coefficient of the cooling fluid when all the other parameters are maintained at design-point values. The TEC power and efficiency improve as the convective-heat-transfer coefficient increases to lower the collector temperature. However, increasing the heat-transfer coefficient over 1000 W/m² K has a negligible effect in the TEC performance enhancement due to full suppression of back electron emission from the collector.
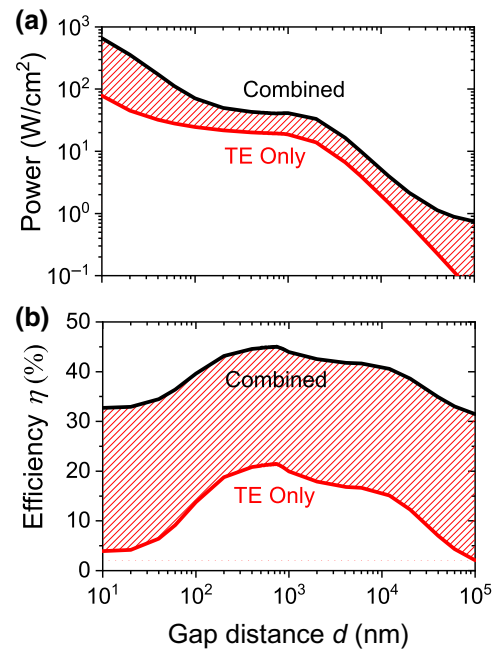

FIG. 7. Increase in (a) the maximum power output and (b) efficiency by combining a TEC cycle with a bottom-cycle heat engine with 30% efficiency. Heat rejection from the collector, ordinarily wasted, is now harnessed to generate additional power in the bottom cycle to improve the system efficiency. The efficiency reaches 48.3% at $d = 730$ nm, and for $d < 100$ nm a power density is generated greater than 100 W/cm² at an efficiency larger than 30%.

The back emission of electrons from the collector becomes significant enough to drop the net thermionic power output almost to zero. On the other hand, increasing the heat transfer to 10^4 W/m² K cools down the collector to 372 K. However, this cooling effect does not noticeably increase the power output and the efficiency, indicating that the work function of the collector (i.e., 1.33 eV) is well optimized to minimize the back emission from the collector at 1000 K: further lowering the collector temperature does not increase the net thermionic current density. Rather, a higher convection-heat-transfer coefficient requires additional pumping power for the cooling fluid, which will reduce the overall system performance.

While stand-alone submicron-gap TEC systems can achieve energy conversion efficiency at 20%–25%, the thermionic collector can be used as a high-quality heat source for combined power generation [46]. Figure 7 shows the increase in power output and efficiency when the TEC device pairs with a conventional power system, such as a steam or Stirling heat engine [19,46], that is assumed to convert heat to electrical power at 30% efficiency. Although only the maximum power case is shown in the figure, the maximum efficiency case shows the same

effect when combined with the bottom power cycle. The TEC system characteristics are $T_E = 1575$ K ($\Phi_E = 2.10$ eV) and $T_C = 1000$ K ($\Phi_C = 1.33$ eV). Both the power output and the efficiency exhibit significant enhancement when compared to the stand-alone TEC device, particularly for gaps less than 1 μm. This enhancement is due to near-field radiative heat transfer from the emitter to the collector. This heat-transfer mechanism delivers a significant amount of Q_{out} to the working fluid of the bottom-cycle heat engine. As a result of combining heat engines, the total power output is more than doubled from 19.3 W/cm² to 40.6 W/cm² at $d = 730$ nm, at which the combined cycle efficiency reaches a maximum of 45.0%. The demonstrated feasibility of forming a tandem heat engine is a compelling advantage of TEC over other solid-state energy conversion schemes that often require the cold side maintained at near room temperature.

Despite the theoretically demonstrated advantages in the present study, experimental verification of submicron-gap thermionic power generation remains unexplored to date. Previous works have measured the effect of reducing a vacuum gap in thermionic-energy-conversion processes [5,9,11]. However, the minimum gap distance achieved to date is 1.8 μm through complex microfabricated spacers

between electrodes [29]. This limitation in the gap distance is mainly due to technical challenges in achieving submicron-gap distances between parallel planar structures. In addition, there has been a lack of evidence on the benefits of achieving such small gaps for thermionic power generation [26]. However, recent progresses have been made to secure vacuum gaps on the order of 100 nm between mm^2-scale area plates, either by implementing microfabricated spacers [47,48] or nanopositioners [49]. As a future research direction, the same strategy can be applied for the measurement of submicron-gap thermionic power generation.

IV. CONCLUSIONS

The present work numerically studies thermionic-energy-conversion processes with an emphasis on comprehensive nanoscale charge- and thermal-transport phenomena. The obtained results demonstrate that submicron-gap TEC can outperform the ideal case having no space-charge effects due to field-induced charge acceleration caused by strong electrostatic interactions from image charges. The systematic energy-balance analysis yields the maximum energy conversion efficiency at around 20%–25% when the device is operated at $T_E = 1575$ K with the vacuum-gap range of 300 nm $\lesssim d \lesssim 1$ μm. This optimum range of gap distances is smaller than the micrometer range previously determined in the literature. We also theoretically predict potential advantages of implementing the TEC device into a combined power-generation cycle. Although the experimental demonstration of the predicted TEC performance still remains for future research, we believe that securing submicron vacuum-gap distances will further enhance the performance of thermionic power generation.

———————————

[1] I. Langmuir, The effect of space charge and initial velocities on the potential distribution and thermionic current between parallel plane electrodes, Phys. Rev. **21**, 419 (1923).

[2] G. N. Hatsopoulos and E. P. Gyftopoulos, *Thermionic Energy Conversion* (MIT Press, Cambridge, Massachusetts, 1973), Vol. 1.

[3] A. Shakouri, in *Proceedings of International Conference on Thermoelectronics* (IEEE, Clemson SC, 2005), p. 492.

[4] E. Skoplaki and J. A. Palyvos, On the temperature dependence of photovoltaic module electrical performance: A review of efficiency/power correlations, Solar Energy **83**, 614 (2009).

[5] J. H. Lee, I. Bargatin, B. K. Vancil, T. O. Gwinn, R. Maboudian, N. A. Melosh, and R. T. Howe, Microfabricated thermally isolated low work-function emitter, J. Microelectromech. Syst. **23**, 1182 (2014).

[6] L. Zhu, A. P. Raman, and S. Fan, Radiative cooling of solar absorbers using a visibly transparent photonic crystal thermal blackbody, Proc. Natl. Acad. Sci. **112**, 12282 (2015).

[7] V. Wilson and J. Lawrence, Thermionic converter surface conditions (Air Force Aero-Propulsion Laboratory, Research and Technology Division, 1964).

[8] R. Becker, Thermionic space power systems review, J. Spacecr. Rockets **4**, 847 (1967).

[9] H. Yuan, D. C. Riley, Z.-X. Shen, P. A. Pianetta, N. A. Melosh, and R. T. Howe, Back-gated graphene anode for more efficient thermionic energy converters, Nano Energy **32**, 67 (2017).

[10] F. A. Koeck and R. J. Nemanich, Substrate-diamond interface considerations for enhanced thermionic electron emission from nitrogen doped diamond films, J. Appl. Phys. **112**, 113707 (2012).

[11] K. A. Littau, K. Sahasrabuddhe, D. Barfield, H. Yuan, Z.-X. Shen, R. T. Howe, and N. A. Melosh, Microbead-separated thermionic energy converter with enhanced emission current, Phys. Chem. Chem. Phys. **15**, 14442 (2013).

[12] M. Suzuki, T. Ono, N. Sakuma, and T. Sakai, Low-temperature thermionic emission from nitrogen-doped nanocrystalline diamond films on n-type Si grown by MPCVD, Diam. Relat. Mater. **18**, 1274 (2009).

[13] J. Voss, A. Vojvodic, S. H. Chou, R. T. Howe, and F. Abild-Pedersen, Inherent Enhancement of Electronic Emission from Hexaboride Heterostructure, Phys. Rev. Appl. **2**, 1 (2014).

[14] H. Kato, D. Takeuchi, M. Ogura, T. Yamada, M. Kataoka, Y. Kimura, S. Sobue, C. E. Nebel, and S. Yamasaki, Heavily phosphorus-doped nano-crystalline diamond electrode for thermionic emission application, Diam. Relat. Mater. **63**, 165 (2016).

[15] E. V. Barmina, A. A. Serkov, E. Stratakis, C. Fotakis, V. N. Stolyarov, I. N. Stolyarov, and G. A. Shafeev, Nano-textured W shows improvement of thermionic emission properties, Appl. Phys. A: Mater. Sci. Process. **106**, 1 (2012).

[16] G. N. Hatsopoulos and E. P. Gyftopoulos, *Thermionic Energy Conversion* (MIT Press, Cambridge, Massachusetts, 1979), Vol. 2.

[17] K. L. Jensen, *Introduction to the Physics of Electron Emission: Theory and Simulation* (John Wiley & Sons, Chichester, UK, 2017).

[18] I. T. Lim, S. A. Lambert, J. L. Vay, and J. W. Schwede, Electron reflection in thermionic energy converters, Appl. Phys. Lett. **112**, 073906 (2018).

[19] G. Xiao, G. Zheng, M. Qiu, Q. Li, D. Li, and M. Ni, Thermionic energy conversion for concentrating solar power, Appl. Energy **208**, 1318 (2017).

[20] S. Meir, C. Stephanos, T. H. Geballe, and J. Mannhart, Highly-efficient thermoelectronic conversion of solar energy and heat into electric power, J. Renewable Sustainable Energy **5**, 043127 (2013).

[21] R. Wanke, G. W. Hassink, C. Stephanos, I. Rastegar, W. Braun, and J. Mannhart, Magnetic-field-free

thermoelectronic power conversion based on graphene and related two-dimensional materials, J. Appl. Phys. **119**, 244507 (2016).

[22] Y. Hishinuma, T. H. Geballe, B. Y. Moyzhes, and T. W. Kenny, Refrigeration by combined tunneling and thermionic emission in vacuum: Use of nanometer scale design, Appl. Phys. Lett. **78**, 2572 (2001).

[23] M. F. O'Dwyer, T. E. Humphrey, R. A. Lewis, and C. Zhang, Efficiency in nanometre gap vacuum thermionic refrigerators, J. Phys. D **42**, 035417 (2009).

[24] T. Zeng, Thermionic-tunneling multilayer nanostructures for power generation, Appl. Phys. Lett. **88**, 153104 (2006).

[25] J. I. Lee, Y. H. Jeong, H. C. No, R. Hannebauer, and S. K. Yoo, Size effect of nanometer vacuum gap thermionic power conversion device with CsI coated graphite electrodes, Appl. Phys. Lett. **95**, 223107 (2009).

[26] J. H. Lee, I. Bargatin, N. A. Melosh, and R. T. Howe, Optimal emitter-collector gap for thermionic energy converters, Appl. Phys. Lett. **100**, 173904 (2012).

[27] Y. Wang, T. Liao, Y. Zhang, X. Chen, S. Su, and J. Chen, Effects of nanoscale vacuum gap on photon-enhanced thermionic emission devices, J. Appl. Phys. **119**, 045106 (2016).

[28] A. Datas and R. Vaillon, Thermionic-enhanced near-field thermophotovoltaics, Nano Energy **61**, 10 (2019).

[29] M. F. Campbell, M. Azadi, Z. Lu, A. G. Eskenazi, A. Jain, J. W. Bang, P. G. Sieg, G. A. Popov, S. M. Nicaise, K. C. Van Houten, F. Schmitt, J. W. Schwede, and I. Bargatin, Nanostructured spacers for thermionic and thermophotovoltaic energy converters, J. Microelectromech. Syst. **29**, 637 (2020).

[30] M. F. O'Dwyer, R. A. Lewis, C. Zhang, and T. E. Humphrey, Electronic efficiency in nanostructured thermionic and thermoelectric devices, Phys. Rev. B **72**, 205330 (2005).

[31] E. L. Murphy and R. H. Good, Thermionic emission, field emission, and the transition region, Phys. Rev. **102**, 1464 (1956).

[32] S. G. Christov, General theory of electron emission from metals, Phys. Status Solidi b **17**, 11 (1966).

[33] K. L. Jensen, Electron emission theory and its application: Fowler–Nordheim equation and beyond, J. Vac. Sci. Technol. B **21**, 1528 (2003).

[34] M. Baeva, Application of the transferred matrix method to a unified evaluation of the cathodic electron emission, AIP Adv. **8**, 85322 (2018).

[35] J. G. Simmons, Electric tunnel effect between dissimilar electrodes separated by a thin insulating film, J. Appl. Phys. **34**, 2581 (1963).

[36] I. Baldea and H. Koppel, Transition voltage spectroscopy in vacuum break junction: The standard tunneling barrier model and beyond, Phys. Status Solidi B **249**, 1791 (2012).

[37] K. Park and Z. M. Zhang, Fundamentals and applications of near-field radiative energy transfer, Front. Heat Mass Transfer **4**, 013001 (2013).

[38] K. Joulain, J.-P. Mulet, F. Marquier, R. Carminati, and J.-J. Greffet, Surface electromagnetic waves thermally excited: Radiative heat transfer, coherence properties and Casimir forces revisited in the near field, Surface Sci. Rep. **57**, 59 (2005).

[39] S. Basu, Z. M. Zhang, and C. J. Fu, Review of near-field thermal radiation and its application to energy conversion, Int. J. Energy Res. **33**, 1203 (2009).

[40] R. Jacobs, D. Morgan, and J. Booske, Work function and surface stability of tungsten-based thermionic electron emission cathodes, APL Mater. **5**, 116105 (2017).

[41] J. L. Stevenson, S. M. Aagesen, R. Lotthammer, and G. Kornfeld, Reliability assessment of dispenser-type thermionic cathodes, Quality Reliability Eng. Int. **4**, 347 (1988).

[42] J. Van Der Maas, R. Huguenin, and V. A. Gasparov, Electron-electron scattering in tungsten, J. Phys. F **15**, L271 (1985).

[43] S. Roberts, Optical properties of nickel and tungsten and their interpretation according to drude's formula, Phys. Rev. **114**, 104 (1959).

[44] See Supplemental Material at http://link.aps.org/supplemental/10.1103/PhysRevApplied.15.024062 for discussions on (1) the effect of electrical lead losses to the thermionic energy conversion efficiency; (2) the effect of the emitter temperature onto the thermionic power generation for micron- and submicron-scale gap distances; (3) the gap-dependent TEC performances for different collector temperatures; and (4) the comparison of the TEC power output with and without the image-charge effect.

[45] T. L. Bergman, F. P. Incropera, D. P. DeWitt, and A. S. Lavine, *Fundamentals of Heat and Mass Transfer* (John Wiley & Sons, Hoboken, NJ, 2011).

[46] J. W. Schwede, I. Bargatin, D. C. Riley, B. E. Hardin, S. J. Rosenthal, Y. Sun, F. Schmitt, P. Pianetta, R. T. Howe, Z.-X. Shen, and N. A. Melosh, Photon-enhanced thermionic emission for solar concentrator systems, Nat. Mater. **9**, 762 (2010).

[47] M. P. Bernardi, D. Milovich, and M. Francoeur, Radiative heat transfer exceeding the blackbody limit between macroscale planar surfaces separated by a nanosize vacuum gap, Nat. Commun. **7**, 1 (2016).

[48] J. DeSutter, L. Tang, and M. Francoeur, A near-field radiative heat transfer device, Nat. Nanotechnol. **14**, 751 (2019).

[49] M. Ghashami, H. Geng, T. Kim, N. Iacopino, S. K. Cho, and K. Park, Precision Measurement of Phonon-Polaritonic Near-Field Energy Transfer between Macroscale Planar Structures under Large Thermal Gradients, Phys. Rev. Lett. **120**, 175901 (2018).